Electronic Supplementary Material (ESI) for Nanoscale.

Supplementary Information for The photothermal nonlinearity in plasmon-assisted photocatalysis

Ieng Wai Un,[a*], Yonatan Dubi[b] and Yonatan Sivan[a]

[a]School of Electrical and Computer Engineering, Ben-Gurion University of the Negev, Israel

[b]Department of Chemistry, Ben-Gurion University of the Negev, Beer-Sheva, 8410501, Israel.

*E-mail: iengwai@post.bgu.ac.il

February 24, 2022

S1 The energy absorbed density accounting for the temperature dependence of the permittivities

In Section 3, we have derived the absorbed power density using the temperature-independent permittivity approximation. In this section, we provide a complete derivation of the absorbed power density accounting for the temperature variation within the heat source and the temperature dependence of the permittivity. This is required when the skin (penetration) depth of the light in the sample is comparable to the sample thickness (for example, when the nanoparticle density is highly dilute, or when the wavelength of the illumination is far away from the resonance wavelength of the NPs). In this case, the heat source density becomes

$$p_{\mathrm{abs}}(\mathbf{r}) = -\int i_{\mathrm{inc}}(\rho,\omega)\frac{\partial\zeta(\rho,z,\omega)}{\partial z}d\omega, \tag{S1}$$

where $\zeta(\rho,z,\omega)$ is an unknown longitudinal spatial profile of the incident illumination which needs to be determined by solving the Beer-Lambert equation for the absorption of light with a space-dependent penetration depth $\delta_{\mathrm{skin}}(T(\mathbf{r}),\omega)$ (elucidated below), namely, $\partial\zeta(\rho,z,\omega)/\partial z = -\zeta(\rho,z,\omega)/\delta_{\mathrm{skin}}(T(\mathbf{r}),\omega)$. This enables us to accommodate the temperature gradient build-up in the catalyst sample under the illumination.

As before, we neglect the temperature non-uniformity within the individual NPs due to their small size and their high thermal conductivity, see justification in Refs. 1, 2. Furthermore, we assume that the temperature varies slowly on a length scale of the illumination wavelength (see justification in Fig. 1(b)). These assumptions allow us to evaluate the temperature dependence of the absorption cross-section using a uniform metal permittivity and a uniform host permittivity, i.e., $\sigma_{\mathrm{abs}}(\omega,T) = \sigma_{\mathrm{abs}}(\varepsilon_m(\omega,T),\varepsilon_h(\omega,T),\omega)$. In this case, the absorption coefficient becomes

$$1/\delta_{\mathrm{skin}}(T,\omega) = n_p\sigma_{\mathrm{abs}}(\varepsilon_m(\omega,T),\varepsilon_h(\omega,T),\omega),$$

in analogy to Eq. (2), and the absorbed power density has a closed form expression

$$p_{\mathrm{abs}}(\rho, z) = \int i_{\mathrm{inc}}(\rho, \omega) n_p \sigma_{\mathrm{abs}}(\omega, T(\rho, z)) e^{-n_p \int_0^z \sigma_{\mathrm{abs}}(\omega, T(\rho, z'))dz'} d\omega. \tag{S2}$$

The temperature distribution is obtained by solving Eq. (3) coupled with Eq. (S2) self-consistently.

S2 Supplemental simulation results for the experiments of Li *et al.* [3]

Fig. S1(a) shows the simulation results of the top (T_1) and the bottom (T_2) surface temperatures for the case where the catalyst sample was illuminated using the blue light source (without resistive heating). One can see that the simulation results demonstrate an excellent match to the experimental data. This indicates that our model is not only able to explain the photothermal nonlinearity observed in the experiment, but also can explain the large temperature difference built up by the illumination (see Section S3.2 below). Fig. S1(b) shows the simulation results of the top (T_1) surface temperature for the cases where the catalyst sample was resistive-heated and was illuminated three different light sources (UV, white and NIR).

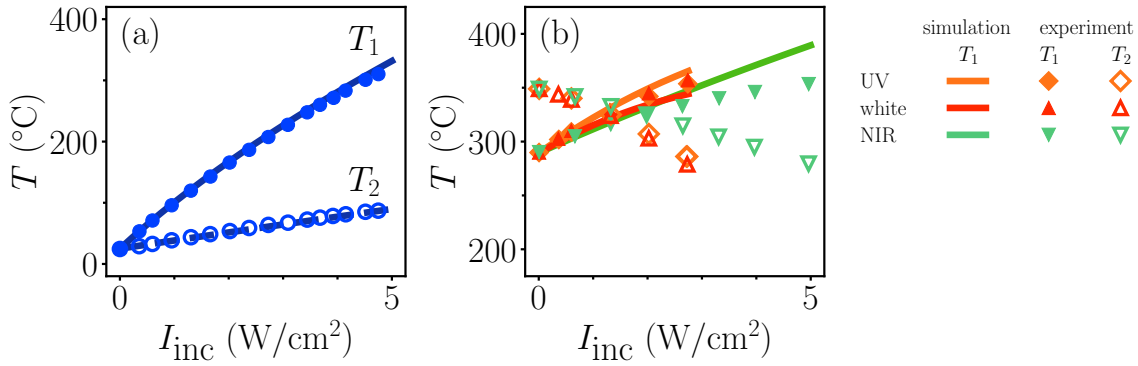

Figure S1: (Color online) The top (T_1) and the bottom (T_2) surface temperatures (the simulation results are represented by the solid and the dashed lines; the experimental data are represented by the solid and the opened symbols.) as a function of the illumination intensity for the blue light source without resistive heating. (b) The same as (a) but under resistive heating. The orange, red and green lines (symbols) represents the simulation results (experimental data) for the UV, white and NIR light sources, respectively.

Fig. S2 shows the comparison between the simulation results (T_1 and T_2) with and without accounting for the thermal emission for the case where the catalyst sample was illuminated using the blue light source. One can see that when the thermal emission is considered in the simulation, the top surface temperature (T_1) is around 8% lower than that without considering the thermal emission. This indicates that the thermal emission plays a minor role on the photothermal nonlinearity. This is mainly because

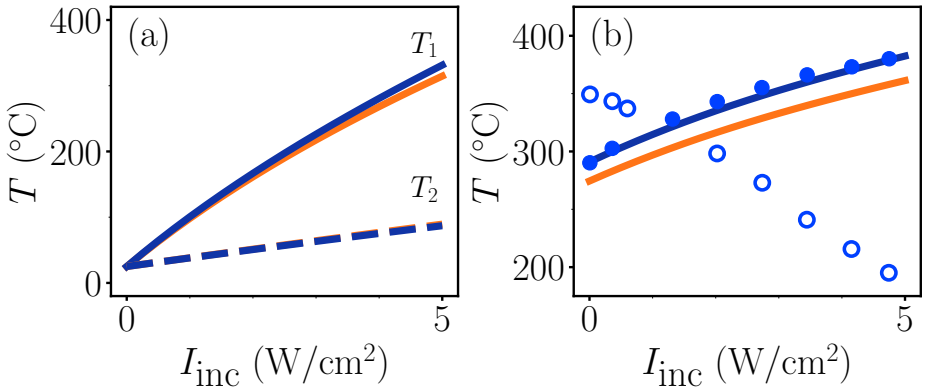

Figure S2: (Color online) The top (T_1) and the bottom (T_2) surface temperatures as a function of the illumination intensity for the blue light source without resistive heating. The blue solid line (T_1) and the blue dashed line (T_2) are the same as Fig. 3(b) represent the results of the simulation results without accounting for the thermal emission. The orange solid line (T_1) and the orange dashed line (T_2) represent the simulation results accounting for the thermal emission. (b) T_1 and T_2 as a function of the illumination intensity for the case where the sample is resistive-heated and is illuminated by the blue light source.

S3 Electromagnetic and thermal simulations

In the experiments [3–5], the catalyst pellet was a mixture of a highly sparse powder of metal nanoparticles and metal oxide microparticles; the gas mixture occupies the empty regions between the various particles. The catalyst pellet sits in a stainless steel sample holder and is put in a reaction chamber, see Fig. 1.

S3.1 Electromagnetic simulations

In the electromagnetic simulations, the absorption of light is modeled using the effective medium approximation for the electromagnetic properties of the catalyst sample, see Section 3 and Eq. (S2).

The absorption cross-section of the NPs is calculated using Mie theory [6] and the bulk permittivity. This could be somewhat inaccurate for NPs of very small sizes (diameter < 10 nm) because the metal permittivity is different from the bulk permittivity due to the nonlocal effect [7, 8]. However, for the conditions under which these experiments are conducted, the penetration depth is much shorter than the sample thickness (see Fig. 2(b) and 4(b)), so that effectively all light that enters the sample gets absorbed. Under these conditions, a change of the absorption cross-section of the NPs would only slightly modify the penetration depth, and will have essentially no effect on the overall temperature distribution in the sample (and hence, on the results in this work).

S3.2 Thermal simulations

The temperature distribution is obtained from the steady-state solution of the heat equation Eq. (3) with temperature-dependent coefficients ($\kappa^{\text{eff}}_{\text{pellet}}(T)$, $\kappa_{\text{gas}}(T)$ and $\kappa_{\text{holder}}(T)$) and subjected to a heat flux boundary condition. As shown in [9], the effect thermal conductivity of the catalyst sample $\kappa^{\text{eff}}_{\text{pellet}}$ can be well described by the Maxwell-Garnett model [10, 11], namely,

$$\kappa^{\text{eff}}_{\text{cata}} = \kappa_{\text{gas}} + \frac{3\kappa_{\text{gas}}(f_{\text{m}} + f_{\text{oxide}})}{\frac{\kappa_{\text{solid}} + 2\kappa_{\text{gas}}}{\kappa_{\text{solid}} - \kappa_{\text{gas}}} - (f_{\text{m}} + f_{\text{oxide}})}, \tag{S3}$$

where f_{m} and f_{oxide} are the metal and the oxide volume fraction in the catalyst pellet, respectively. κ_{gas} is the thermal conductivity of the gas and κ_{solid} is the effective thermal conductivity of the solid material which itself can be again approximated by Maxwell-Garnett model [10, 11]

$$\kappa_{\text{solid}} = \kappa_{\text{oxide}} + \frac{3\kappa_{\text{oxide}}\dfrac{f_m}{f_{\text{m}} + f_{\text{oxide}}}}{\dfrac{\kappa_{\text{m}} + 2\kappa_{\text{oxide}}}{\kappa_{\text{m}} - \kappa_{\text{oxide}}} - \dfrac{f_m}{f_{\text{m}} + f_{\text{oxide}}}}, \tag{S4}$$

where κ_{m} and κ_{oxide} are the metal thermal conductivity and the oxide thermal conductivity, respectively. The volume fraction of the metal and of the oxide can be deduced from the mass (m_{cata})

and the volume V_{cata} of the pellet,

$$\begin{cases} f_{\text{m}} = \dfrac{m_{\text{cata}} w_{\text{m}}/\rho_{\text{m}}}{V_{\text{cata}}}, \\ f_{\text{m}}\rho_{\text{m}} + f_{\text{oxide}}\rho_{\text{oxide}} + (1 - f_{\text{m}} - f_{\text{oxide}})\,\rho_{\text{gas}} = \dfrac{m_{\text{cata}}}{V_{\text{cata}}}, \end{cases} \tag{S5}$$

where w_m is the weight percentage of the metal, ρ_{m}, ρ_{oxide} and ρ_{gas} are the mass densities of the metal, of the oxide and of the gas, respectively. Since the metal volume fraction is usually much smaller than the oxide volume fraction (i.e. $f_{\text{m}} \ll f_{\text{oxide}}$), the effective thermal conductivity of the solid material is dominated by the thermal conductivity of the oxide (i.e. $\kappa_{\text{solid}} \approx \kappa_{\text{oxide}}$), justifying the ignorance of the metal NPs in Section 3. More importantly, since the metal nanoparticles and the metal oxide microparticles have a very small occupation fraction (i.e. $f_{\text{m}} + f_{\text{oxide}} \ll 1$) and since the thermal conductivity of the oxide is much larger than that of the gas (i.e. $\kappa_{\text{oxide}} \gg \kappa_{\text{gas}}$), Eq. (S3) becomes

$$\kappa_{\text{cata}}^{\text{eff}} \approx (1 + 3f_{\text{oxide}})\,\kappa_{\text{gas}} \tag{S6}$$

so that the thermal conductivity of the pellet is very close to that of the gas mixture and is much smaller than that of the oxide, as shown in Fig. S3[1].

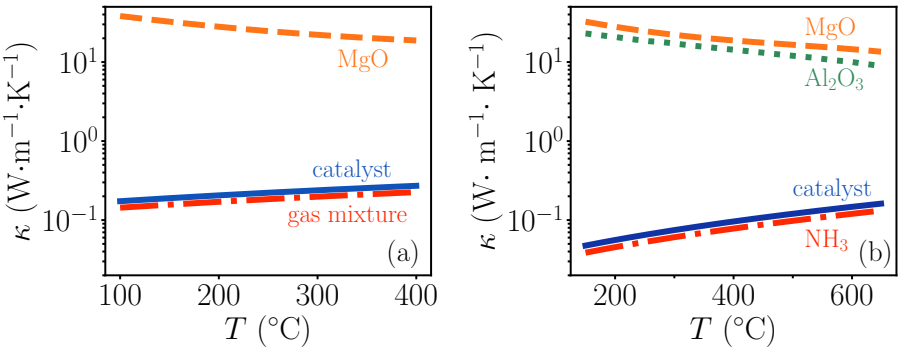

Figure S3: (Color online) The temperature dependence of the thermal conductivities assigned to the simulations for (a) the experiment in [3] and (b) the experiment in [5].

The thermal conductivity of gases can be understand using the kinetic theory of gases [14]. For

[1]The thermal conductivities of MgO and of Al_2O_3 are taken from [12] and [13], respectively.

ideal gases, the thermal conductivity is given by

$$\kappa_{\text{ideal gas}} = \frac{f}{3D^2}\sqrt{\frac{k_B^3 T}{\pi^3 M}}, \tag{S7}$$

where f is the number of degrees of freedom, D is the collision diameter, M is the molecule mass and k_B is the Boltzmann constant. Thus, the thermal conductivity of ideal gases increases with the temperature because the gas molecules collide with each other and transfer energy more frequently at high temperatures. For the same reason, the thermal conductivity of gases with lighter molecules is higher than that of gases with heavier molecules. Moreover, gases with larger molecules have lower thermal conductivity than gases with smaller molecules because of their larger collision diameter. When the gas is a mixture of reactants, products and carrier gas, the thermal conductivity of the gas mixture can be calculated using $\kappa_{\text{gas mixture}} = \sum_i x_i \kappa_i$, where x_i and κ_i are the mole fraction and the thermal conductivity of the i-th gas.

Next, we need to understand the efficiency of the sampler holder in releasing heat. To do that, we discuss separately the two experimental conditions - when the catalyst sample is not being resistive-heated and when it is.

For experiments where the catalyst sample is resistive-heated, the sample holder temperature is controlled by the heater which is connected to the sample holder. In that sense, the sample holder serves only as a sort of "boundary condition" and its thermal conductivity is of no consequence. For the same reason, in this case the temperature dependence of the thermal conductivity of the sample holder cannot play any significant role on the photothermal nonlinearity.

For experiments where the catalyst sample is not resistive-heated, since the heat generation occurs primarily on the top layer of the catalyst, i.e., away from most of the sample holder, the sample holder plays a minor role. To see that, we performed a simulation where no holder is included and the sample is levitating as shown in Fig. S4(a). The simulation results of T_1 and T_2 for the levitating sample are shown in Fig. S4(b) and are compared with the results of the simulation where the holder was included. The simulation results show that when the holder is included, for the illumination intensity of 5 W/cm^2 T_2 is reduced from $\sim$ 215°C to $\sim$ 90°C whereas T_1 is reduced from $\sim$ 385°C to $\sim$ 310°C. This indicates that the sample holder is effective to

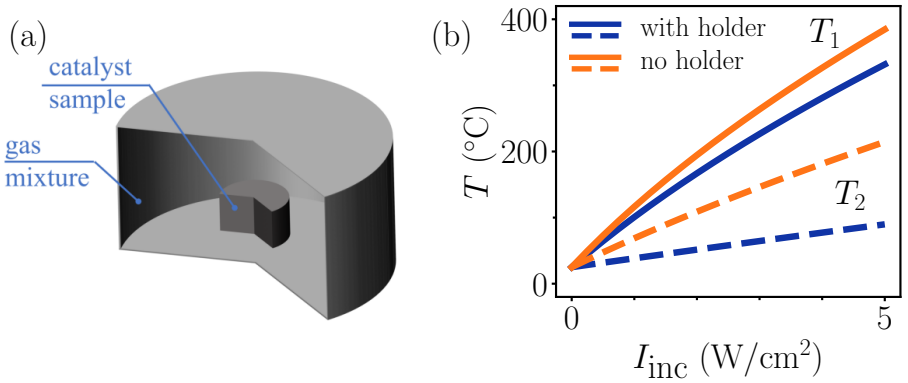

Figure S4: (a) Schematic illustrations of the photocatalytic chamber without considering the steel holder, i.e. the photocatalyst sample is levitating. (b) T_1 and T_2 as a function of the illumination intensity. The blue solid line (T_1) and the blue dashed line (T_2) are the same as Fig. 3(b), representing the results of the simulation where the holder was included. The orange dotted solid line (T_1) and the dash-dotted line (T_2) representing the results of the simulation where the sample is levitating (no holder).

reduce the bottom-surface temperature but is less effective to reduce the top-surface temperature. Moreover, since the increase of the holder temperature (which is almost equal to T_2) is much smaller than the that of the top-surface temperature T_1 when the illumination intensity increases (see Fig. 3(b)), and since the temperature dependence of the thermal conductivity of the sample holder [2] is 2.5 to 4 times weaker than that of gases, the sample holder plays only a minor role on the photothermal nonlinearity.

Finally, the heat transfer from the chamber to the outer environment is modelled using a heat flux boundary condition driven by the temperature difference between the chamber boundary and the outer environment $h(T_{\rm boundary} - T_{\rm env})$. Therefore, a smaller value of h gives rise to a stronger linear photothermal response. Based on this understanding, one can determine the value of h by fitting the simulation results to the results of the experiments where the catalyst sample is not being resistive-heated and small intensity limit, see e.g. Fig. 3(b). In Fig. S5, we plot the simulation results for the experiment [3] using different values of h (35 W/(m$^2\cdot$ K), 70 W/(m$^2\cdot$ K) and 140 W/(m$^2\cdot$ K)). One can see that the simulation results of T_1 and T_2 are weakly sensitive to the value of h. Moreover, the value of h ensures that the rate of the illumination energy absorbed by the catalyst sample is equal to the rate of the thermal energy released to the outer environment

[2]The thermal conductivity of the steel support is [15] $\kappa_{\rm steel}(T) = 14.6 + 1.27\times10^{-2}T$, where $\kappa_{\rm steel}$ is in W/(m·K) and T is in °C.

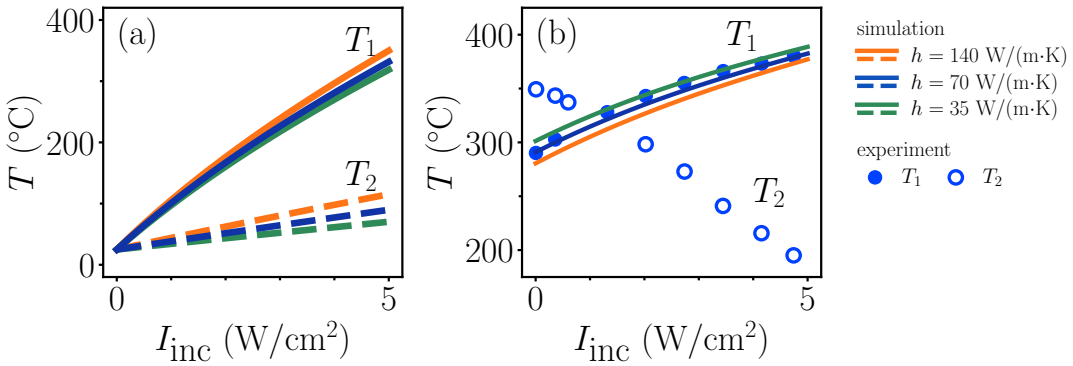

Figure S5: (Color online) (a) T_1 and T_2 as a function of the illumination intensity for the case where the sample is not resistive-heated. The blue solid line (T_1) and the blue dashed line (T_2) are the same as Fig. 3(b), represent the results of the simulation where h is set to be 70 W/(m^2·K). The orange (green) solid line and the orange dashed (green) line represent the results of the simulation where h is set to be 140 W/(m^2·K) (35 W/(m^2·K)). (c) the same as (b), T_1 and T_2 as a function of the illumination intensity for the case where the sample is resistive-heated and is illuminated by the blue light source.

through the boundary. For example, when the illumination intensity is 1 W/cm^2, the side boundary temperature is around 1°C higher than the T_{env} whereas the average temperature of the top- and of bottom-boundary are around 5.5°C higher than the T_{env}, so that the releasing rate of the thermal energy is around $hA_{\text{side}}(T_{\text{side}}-T_{\text{env}})+hA_{\text{top}}(T_{\text{top}}-T_{\text{env}})+hA_{\text{bottom}}(T_{\text{top}}-T_{\text{env}}) \approx 0.285$W for $h \approx 70$ W/(m^2·K), here A_{side}, A_{top} and A_{bottom} are the area of the side-, of the top- and of the bottom-boundary, respectively. This is in agreement with the rate of energy absorbed by the sample 0.283W. Moreover, once the value of h is determined, it plays nearly no role on the nonlinear photothermal response. Finally, the value of T_{env} was taken to be 20°C. This is equal to the catalyst temperature when the catalyst sample is not resistive-heated and there is no illumination.

S4 Supplemental simulation results for the experiments of Zhang *et al.* [4]

We adapt the simulation configuration used in Section 4.1 to the experimental setup described in [4] and simulate the temperature distribution using the heat transfer module of COMSOL Multiphysics. The thermal conductivity of the input gases [16–18] and of their mixture are shown in Fig. S6(a). The catalyst sample was 1 mm thick and was illuminated by a UV light source

(365 nm). The penetration (skin) depth to the sample is calculated using the permittivity data of Rh [19]. We again find that the penetration depth is much smaller than the sample thickness.

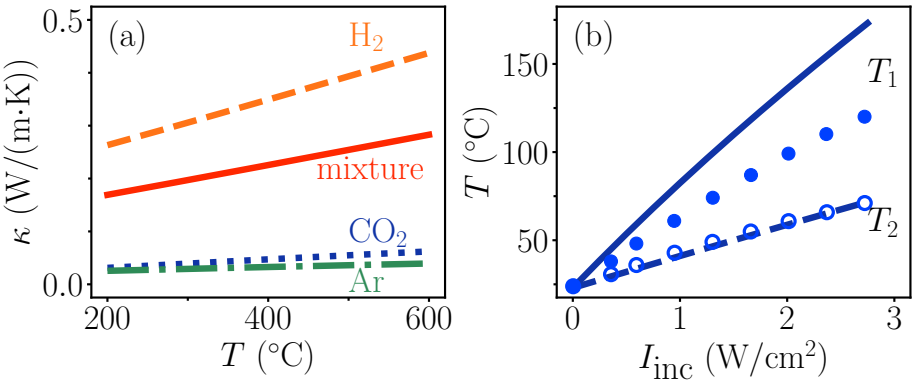

Figure S6: (Color online) (a) Temperature dependence of the thermal conductivities of CO_2 [16], of H_2 [17], Ar [18] and the mixture used in Ref. [4]. (b) T_1 and T_2 as a function of the illumination intensity for the experiment without resistive heating in Ref. [4]. The solid and dashed lines represent the COMSOL simulation results, and the symbols are extracted from Ref. [4].

Fig. S6 shows the simulation results of the top (T_1) and bottom (T_2) surface temperatures for the experiments without the resistive heating in Ref. [4]. One can see that the simulation result of T_1 is around 50°C higher than the experimental data at the illumination intensity of 2.75 W/cm^2. Since a large gas flow (250 sccm) was used in the experiment [4] (which is $>$ 3 times larger than that (75 sccm) used in [3]), the gas mixture becomes more efficient in releasing heat. In this respect, using the non-convection approximation is one possible reason for the small between the simulation results and the experimental data.

S5 Temperature dependence thermal conductivity in the experiments of Xu *et al.* [20]

Recently, Xu *et al.* [20] studied the temperature non-uniformity in alumina-supported ruthenium catalysts under illumination using fiber Bragg grating sensors. Based on the energy balance for the top surface of the catalyst sample, the authors attributed the observed photothermal nonlinearity to the thermal emission even at relatively weak illumination levels. As mentioned in the main text, this is mainly because the emissivity of alumina is relatively high at 25-400°C [21]. Here, we

extend the analysis of [20] in order to demonstrate that it confirms the main conclusions of our analysis. To demonstrate that, we first obtain the temperatures at different depths in the catalyst sample under different illumination intensities from Fig. 2b in [20]. Next, we perform a linear fit to the data. This immediately gives us the temperature gradients of 64 K/mm, 94 K/mm, 112 K/mm and 118 K/mm at the illumination intensities of 0.5 W/cm^2, 1 W/cm^2, 1.6 W/cm^2 and 2.25 W/cm^2, respectively (see Fig. S7(a)). Then, we employ the energy balance for the top surface of the catalyst sample proposed in [20] to calculate the effective thermal conductivity of the catalyst sample, as shown in Fig. S7(b). This analysis shows that the effective thermal conductivity of the catalyst sample increases with temperature and is comparable to thermal conductivities of gases, in line with the analysis in Section 2. More importantly, this indicates that the observed nonlinear temperature rise in [20] is not only caused by the thermal emission but also the temperature-dependence of the effective thermal conductivity.

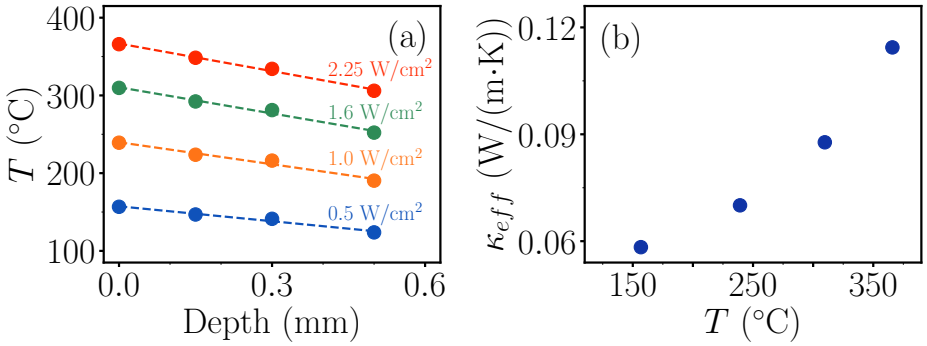

Figure S7: (Color online) (a) The temperature at different depths in the catalyst sample at illumination intensities 0.5 W/cm^2 (blue), 1 W/cm^2 (orange), 1.6 W/cm^2 (green) and 2.25 W/cm^2 (red), extracted from Fig. 2b in [20]. The dashed lines are the linear fits to the corresponding data. (b) The calculated effective thermal conductivity of the catalyst sample based on the energy balance for the top surface of the catalyst sample.

S6 Description of the COMSOL simulation file

In this section, we provide the detailed description of the attached COMSOL simulation file. As mentioned in the main text, the simulation includes the catalyst sample, the sample holder and the reaction chamber with a few simplification. The geometry parameters are listed in the "Description" column of the "Global definition - Parameters" section. The temperature-dependent thermal

conductivity of the gas mixture (the red line in Fig. 4(a)) is fitted using a polynomial of degree 3 and then is imported to the "Component 1 - Materials" section. The temperature-dependent thermal conductivity of the catalyst sample is defined based on Eq. (5). The illumination induced heat sources as a function of z (normalized to 1 W/m^2) are calculated using Eq. (4) [3] and are defined in the "Global definition" section as "htsc365", "htsc455", "htscNIR" and "htscWHT" for the UV (365 nm), blue (455 nm), NIR and white light sources, respectively. The heat source is imposed to the catalyst sample by setting the "General source" to be "ity $*$ htscXXX(z)" in "Component 1 - Heat transfer in Fluids - Heat source 1" section, where "ity" is the illumination intensity and "htscXXX" is "htsc365", "htsc455", "htscNIR" or "htscWHT". In addition, a temperature boundary condition "T2" is set to control the bottom temperature of the catalyst sample to mimic the resistive heating, as mentioned in the main text. One needs to enable/disable the temperature boundary condition "T2" when running the simulation that the catalyst sample is/is not under resistive heating. "Study Blue 455", "Study UV 365", "Study NIR" and "Study WHT" are set in the model to simulate the temperature distribution for the blue, UV, NIR and white light sources, respectively. In each "Study", a "Parametric Sweep" is set to vary the illumination intensity "ity". When running the simulation for the catalyst sample under resistive heating, the "Parametric Sweep" is also set to vary "T_2" simultaneously. Here, T_2 is extracted from Fig. S6 in Ref. [3]. When running the simulation for different light sources, one needs to use the corresponding heat source function "htscXXX" in "Heat source 1" section.

References

[1] G. Baffou, R. Quidant and F. J. G. de Abajo, *ACS Nano*, 2010, **4**, 709–716.

[2] I. W. Un and Y. Sivan, *J. Appl. Phys.*, 2019, **126**, 173103.

[3] X. Li, X. Zhang, H. O. Everitt and J. Liu, *Nano Lett.*, 2019, **19**, 1706–1711.

[4] X. Zhang, X. Li, M. E. Reish, D. Zhang, N. Q. Su, Y. Gutiërrez, F. Moreno, W. Yang, H. O. Everitt and J. Liu, *Nano Lett.*, 2018, **18**, 1714–1723.

[3] light source spectra are extracted from Fig. S2 in Ref. [3].

[5] L. Zhou, D. F. Swearer, C. Zhang, H. Robatjazi, H. Zhao, L. Henderson, L. Dong, P. Christopher, E. A. Carter, P. Nordlander and N. J. Halas, *Science*, 2018, **362**, 69.

[6] C. F. Bohren and D. R. Huffman, *Absorption and scattering of light by small particles*, Wiley & Sons, 1983.

[7] F. J. García de Abajo, *The Journal of Physical Chemistry C*, 2008, **112**, 17983–17987.

[8] C. David and F. J. García de Abajo, *The Journal of Physical Chemistry C*, 2011, **115**, 19470–19475.

[9] A. V. Gusarov and E. P. Kovalev, *Phys. Rev. B*, 2009, **80**, 024202.

[10] R. B. Bird, W. E. Stewart and E. N. Lightfoot, *Transport Phenomena 2nd edition,(2002)*.

[11] K. Pietrak and T. S. Wísniewski, *J. Power Technol.*, 2014, **95**, 14–24.

[12] D. C. Harris, L. R. Cambrea, L. F. Johnson, R. T. Seaver, M. Baronowski, R. Gentilman, C. Scott Nordahl, T. Gattuso, S. Silberstein, P. Rogan, T. Hartnett, B. Zelinski, W. Sunne, E. Fest, W. Howard Poisl, C. B. Willingham, G. Turri, C. Warren, M. Bass, D. E. Zelmon and S. M. Goodrich, *Journal of the American Ceramic Society*, 2013, **96**, 3828–3835.

[13] T. Takeuchi, *Science and Technology of Advanced Materials*, 2014, **15**, 064801.

[14] F. W. Sears and G. L. Salinger, *Thermodynamics, kinetic theory, and statistical thermodynamics*, Addison-Wesley, Boston, MA, 3rd edn, 1975.

[15] J.-M. Franssen and P. Vila Real, *Fire Design of Steel Structures*, John Wiley & Sons, Ltd, Hoboken, NJ, 2nd edn, 2016.

[16] Engineering ToolBox, *Carbon dioxide - Thermal Conductivity*, 2018.

[17] Engineering ToolBox, *Hydrogen - Thermal Conductivity*, 2018.

[18] S. C. Saxena and S. H. P. Chen, *Molecular Physics*, 1975, **29**, 1507–1519.

[19] S. Adachi, *The Handbook on Optical Constants of Metals*, World Scientific, 2012.

[20] Z. M. Xu, T. den Hartog, L. Cheng, M. Wolfs, R. Habets, J. Rohlfs, J. van den Ham, N. Meulendijks, F. Sastre and P. Buskens, *ChemPhotoChem*, 2022, e202100289.

[21] Mikron Instrument Company, Inc., *Table of Emissivity of Various Surfaces for Infrared Thermometry*, 2018.